Composites & nanocomposites

Insights into the complementary behaviour of Gd doping in GO/Gd/ZnO composites as an efficient candidate towards photocatalytic degradation of indigo carmine dye

Samuel Osei-Bonsu Oppong[1,2,*], Francis Opoku[2,*] , William Wilson Anku[3], and Penny P. Govender[2]

[1] Marine Engineering Department, Regional Maritime University, P.O. Box GP 1115, Accra, Ghana

[2] Department of Chemical Sciences (Formerly Department of Applied Chemistry), University of Johannesburg, Doornfontein Campus, P.O. Box 17011, Johannesburg 2028, South Africa

[3] CSIR-Water Research Institute, P.O. Box M.32, Accra, Ghana

ABSTRACT

Water pollution caused by the discharge of hazardous organic pollutants from the food, textile, leather and paper industries is becoming a task for sustainable development. Photocatalysis is considered to be an effective method for removing organic contaminants from dye wastewater. The photocatalytic activity of ZnO-based catalyst based on its ability to generate electron–hole pairs upon photoillumination is limited due to its wide bandgap. In this study, novel GO/Gd/ZnO composites with varying percentages (0.3–1%) of Gd were fabricated via a hydrothermal approach and their photocatalytic degradation processes and performance of indigo carmine (IC) dye were investigated under light irradiation. The chemical composition and morphological features of the prepared GO/Gd/ZnO composites were characterized by X-ray diffraction, scanning electron microscopy, transmission electron microscope, energy-dispersive spectroscopy, Brunauer–Emmett–Teller, Raman and Fourier–transform infrared spectroscopy. GO/Gd/ZnO composites show much higher photocatalytic performance with complete IC dye degradation within 30 min of irradiation than bulk ZnO and GO/ZnO composite. Moreover, the optimal performance was revealed by the GO/Gd/ZnO (0.6% Gd) composite (nearly 96% degradation of IC dye). Using density functional theory, we explore the potential drop across the interface, electronic and structural properties of GO/ZnO and GO/Gd/ZnO composites. The photodegradation rate of IC dye by GO/Gd/ZnO (0.6% Gd) composite was 7.65 and 2.94-fold higher than those of

Address correspondence to E-mail: samuel.oppong@rmu.edu.gh; ofrancis2010@gmail.com

Springer

bulk ZnO and GO/ZnO composite. The capture experiments revealed $^{\cdot}O_2^{-}$ and $^{\cdot}OH$ as the main active radicals during the photodegradation process. The theoretical and experimental findings obtained in this study indicate that GO/Gd/ZnO photocatalyst has great potential application for eliminating environmental pollutants.

Introduction

The continuing growth of urbanization and industrialization produces huge volumes of wastewater containing organic pollutants, such as microbial pathogens, heavy metals, toxic organics, phenolic compounds, dyes, insecticides and pesticides. Among them, synthetic dyes have widespread use in several industries, including pharmaceuticals, food, leather, paper printing, cosmetics and textile [1, 2], where dyes are produced on a large scale. Effluents of refractory organic dyes containing benzene rings released into wastewater cause environmental pollution and severe health hazards to human beings [3]. Most synthetic dyes, even at very low levels, are harmful to human health, aquatic, and microorganism's life, as they are mutagenic and carcinogenic [4, 5]. Conventional techniques, such as anaerobic biological treatment, ozonization, ultrafiltration, membrane technology, chemical oxidation, adsorption, ion exchange, precipitation, reverse osmosis and electrochemical treatment used to treat industrial wastewater [6], have limitation, such as high operating cost, energy consumption and production of toxic by-products [7]. Hence, there is a need to develop economically and sustainably practicable technology to treat, recycle, and reuse wastewater containing environmentally benign, time-saving, clean and inexpensive dyes.

Much research has recently been devoted to developing an up-and-coming technique for the treatment of industrial wastes and organic pollutants through advanced oxidation processes (AOP) under simulated light irradiation [8]. Among these AOPs, heterogeneous semiconductor photocatalysts like tin oxide (SnO_2), titanium dioxide (TiO_2) and zinc oxide (ZnO) considered as a non-hazardous, stable, cheap, chemically and biologically inert, green, promising and convenient technology in water/wastewater treatment can effectively degrade organic pollutants into mineral acids, H_2O and CO_2 without producing secondary pollutants [9]. Among the different semiconductors, ZnO is a promising material for the photodegradation of organic dyes due to its easy tunability of the surface structure, high electron mobility (205–1000 cm^2 V^{-1} s^{-1}), straightforward tailoring of the nanostructures, large excitation binding energy (60 meV) and non-toxicity [10]. However, ZnO has a limitation in several industrial applications because of its large bandgap gap (3.37 eV), which comprises only 4% of the total solar spectrum and the fast recombination rate of charge carriers [11]. A significant number of effective possible solutions, such as doping with non-metal and metal impurities, incorporating metal ions, constructing a heterojunction, creating different nanostructures and using dye sensitizers have been developed to enhance the visible light response of bulk ZnO [12].

Heterojunction construction of two or more semiconductors can form an electric field to accelerate the separation of photogenerated charge carriers on the ZnO surface [13, 14], thereby improving the photocatalytic performance [15]. To accomplish this, ZnO was coupled with carbon materials like graphene oxide (GO), graphene, carbon nanotubes and graphitic carbon nitride [16, 17]. Due to the specific surface area, chemical durability and higher conductivity, GO is suitable for ZnO to enhance its photoactivity [18, 19]. GO possesses an apparent bandgap due to its functionalization with large oxygen-containing groups. This allows it to couple with several semiconductors via covalent and/or ionic bonds to form a composite [20]. These oxygen-containing functional groups serve as binding sites to positively charged ions to be adsorbed on its surface. GO-based composites have been increasingly explored in applications, such as CO_2 reduction, organic pollutant degradation and H_2 generation [21–23]. Moreover, doping of ZnO with rare earth (RE) ions has been used as a strategy to improve its intrinsic photocatalytic performance [24, 25]. Doping is a suitable method that yields remarkable

morphological, catalytic, electrical and optical properties [26–28]. The higher activity is because of the electron transition in 4f layer of RE [29], which reduces the bandgap and improves the separation of charge carriers [30]. Lanthanide-doped inorganic materials can transform low energy photons into higher energy photons via a multiphoton absorption process [31] and have been extensively used in medical imaging and drug delivery fields, biosensing, multicolour displays and solar cells [32].

Over the past few years, the fabrication of hierarchical nanostructures has been an area of interest as it provides several advantages, such as light-harvesting and enhanced photocatalytic activity [33]. Herein, using the hydrothermal method, GO/Gd/ZnO composites were prepared using GO, hydrated gadolinium nitrate, and ZnO as the starting materials. To the best of our knowledge, this is the first time the photoactivity of GO/Gd/ZnO composites against indigo carmine (IC) dye under visible light illumination was investigated. Gd^{3+} ions could be used as a sensitizer due to their high visible light absorption. The light absorption properties, morphology and crystal structure of the as-fabricated catalysts were characterized. Moreover, we have systematically investigated the potential drop across the interface, electronic and structural properties of GO/ZnO and GO/Gd/ZnO composites using density functional theory (DFT) simulations. The dynamic stability and van der Waals (vdWs) force between layers were verified by calculating the electron localization function and phonon dispersion. To investigate interfacial charge transfer, the Löwdin charge population analysis and charge density difference were carried out. Our findings offer theoretical insights into the experimental synthesized GO/ZnO and GO/Gd/ZnO composites.

Experimental details

Preparation of photocatalysts

All chemical reagents and solvents were bought from Sigma-Aldrich and used as received without further purification. Deionized water was used to prepare all aqueous solutions for the photocatalytic experiments. GO was fabricated from natural graphite using modified Hummer's method [34], which was also used in our previous studies [35–38]. 0.04 g GO

sheets were dispersed in 100 ml water for around 30 min. Then, About 10 g of hydrated zinc nitrate $[Zn(NO_3)_2.6H_2O]$ and various masses of hydrated gadolinium nitrate $[Gd(NO_3)_3.6H_2O]$ was added in a well-dispersed GO aqueous solution at room temperature with vigorous magnetic stirring to form a homogeneous solution. To the resulting mixture, 3 M NaOH solution was slowly added into the as-obtained solution until reaching pH 10 and was then hydrothermally treated to 130 °C for 12 h. The white precipitate was collected and washed several times with DI and anhydrous ethanol. The washed precipitate was then sonicated in an ultrasonic bath for 5 h at 50 °C. The above preparation steps of GO/Gd/ZnO then follow to prepare ZnO and GO/ZnO without the addition of $Gd(NO_3)_3.6H_2O$ and both $Gd(NO_3)_3.6H_2O$ and GO, respectively.

Photocatalytic experiments

The performance of the as-prepared composites towards the photodegradation of aqueous solution of IC dye under simulated solar light was evaluated by adding 100 mg of the prepared photocatalysts into 100 mL of IC dye solution (20 mg L^{-1}) and magnetically stirred for 1 h in the dark to establish adsorption–desorption equilibrium before irradiation. During the photodegradation of IC dye, aliquots of 5 mL were taken out from the solution every 30 min using a disposal syringe containing a filtered membrane of 4 μm for 210 min. The IC dye concentrations were obtained by monitoring the absorbance at 610 nm using a Full-Spectrum Solar Simulator (Newport, Model: 9600). The light source was 150 W Xe arc lamp and the illumination intensity of the light source was 100 mW cm^{-2}. The distance between the dye liquid level and the light source was 33 mm. The temperature was maintained at 25 °C using circulating water. The degradation efficiency was defined by the C/C_0, where C is the concentration at degradation time t and C_0 is the initial concentration of IC at $t = 0$. The same reaction conditions were used to recycle and reuse the photocatalysts for five cycles.

Identification of reactive species

The reactive oxidative species involved in the photocatalytic IC dye degradation was investigated by trapping experiment using benzoquinone (BQ), isopropanol (IPA) and ammonium oxalate (AO) as

scavengers of superoxide radicals $(\dot{O_2}^-)$, hydroxyl radicals $(\dot{OH})$ and holes (h^+). The trapping experiment was very similar to the photodegradation experiment, but a suitable amount of quenchers was added before the addition of photocatalyst in the dye solution. The generation of reactive oxygen species was obtained by adding 10 mL of active species scavenger (5 mmol) to IC dye solution containing GO/Gd/ZnO (0.6% Gd) composite.

Characterization

X-ray diffractometer (Philip's X-ray diffraction) was used to study the X-ray diffraction (XRD) patterns of the as-fabricated photocatalysts at 30 mA and 40 kV with Cu Kα radiation (λ = 0.15406). Infrared spectra were recorded on the PerkinElmer Fourier-transform infrared spectroscopy (FTIR) (Spectrum 100) in the wavelength range of 400–4000 cm^{-1} and the Raman spectra on PerkinElmer Raman microscope (Raman Micro 200). The optical property was recorded using Shimadzu UV-2540 (Japan) UV–visible diffuse reflectance spectroscopy. The specific surface area was assessed using the Brunauer–Emmett–Teller (BET) measurement. Transmission electron microscopy (TEM) and scanning electron microscopy (SEM) images were obtained on JEOL JEM-2100F and TESCAN (Vega 3 XMU) microscope at an accelerating voltage of 200 and 15 kV, respectively. The elemental composition of the composites was obtained by energy-dispersive X-ray spectroscopy (EDX) attached to SEM.

Computational method

All simulations were performed using the plane-wave DFT within the Quantum Espresso package (version 6.4.1) [39, 40] and norm-conserving Vanderbilt pseudopotentials [41]. The generalized gradient approximation developed by Perdew–Burke–Ernzerhof [42] was employed to describe the electron exchange–correlation potentials and the DFT-D3 method of Grimme was used to describe the vdWs interactions between the layers [43]. The kinetic energy cut-off for the plane-wave expansion was set to 40 Ry (charge density of 340 Ry) and the k-point grid of $8 \times 8 \times 1$ was used for the Brillouin zone sampling using the Monkhorst–Pack mesh [44]. All the structures were fully relaxed until the energy and force were converged to 10^{-5} Ry and 10^{-3} Ry Bohr^{-1},

respectively, under the Broyden–Fletcher–Goldfarb–Shanno algorithm [45]. The vacuum region of about 20 Å in the z-direction was used to separate the interactions between neighbouring slabs. The phonon dispersion calculation was carried out using the density functional perturbation theory [46]. All the optimized structures were visualized using VESTA [47].

To confirm the structural stability, we further calculate the interface adhesion energy (E_{ads}) as follows:

$$E_{ads} = \left(E_{GO/ZnO} - E_{ZnO} - E_{GO}\right)/S \qquad (1)$$

$$E_{ads} = \left(E_{GO/Gd/ZnO} - E_{Gd/ZnO} - E_{GO} - \mu Gd + \mu Zn\right)/S, \qquad (2)$$

where $E_{GO/ZnO}$, E_{ZnO}, $E_{Gd/ZnO}$, E_{GO} and $E_{GO/Gd/ZnO}$ are the total energies of the GO/ZnO, ZnO, Gd/ZnO, GO and GO/Gd/ZnO composites, respectively. μGd and μZn represent the chemical potentials of the Gd dopant and host Zn, respectively. S stands for the contact area of the composites. The charge density difference ($\Delta\rho$) on the isosurface was used to demonstrate the charge transferred between the components in the composite, as follows:

$$\Delta\rho = \rho_{GO/ZnO} - \rho_{ZnO} - \rho_{GO}, \qquad (3)$$

$$\Delta\rho = \rho_{GO/Gd/ZnO} - \rho_{Gd/ZnO} - \rho_{GO}, \qquad (4)$$

where $\rho_{GO/ZnO}$, ρ_{ZnO}, ρ_{GO}, $\rho_{GO/Gd/ZnO}$ and $\rho_{Gd/ZnO}$ are the total charge density of the GO/ ZnO, ZnO, GO, GO/Gd/ZnO and Gd/ZnO, respectively.

Results and discussion

FTIR analysis

FTIR analysis was also used to fully monitor the functional groups and available bonds of the as-prepared catalysts. FTIR spectra of GO, ZnO, GO/ZnO and GO/Gd/ZnO samples were further analysed (Fig. 1a).

The absorption band at 1079, 1381, 1634 and 1716 cm^{-1} was assigned to the v(C–O) stretching vibrations mode, O–H deformation of C–OH group, in-plane vibration from (C=C) bonds and stretching vibrations of –COOH group, respectively [34, 48]. The peak at 494, from 1388 to 1626 and the 3466 cm^{-1} was related to bending vibration of Zn–O bonding, organic impurities from zinc precursors and the adsorption of surface hydroxyl groups. However,

Figure 1 a FTIR and **b** XRD spectrum of GO, ZnO, GO/ZnO and GO/Gd/ZnO samples.
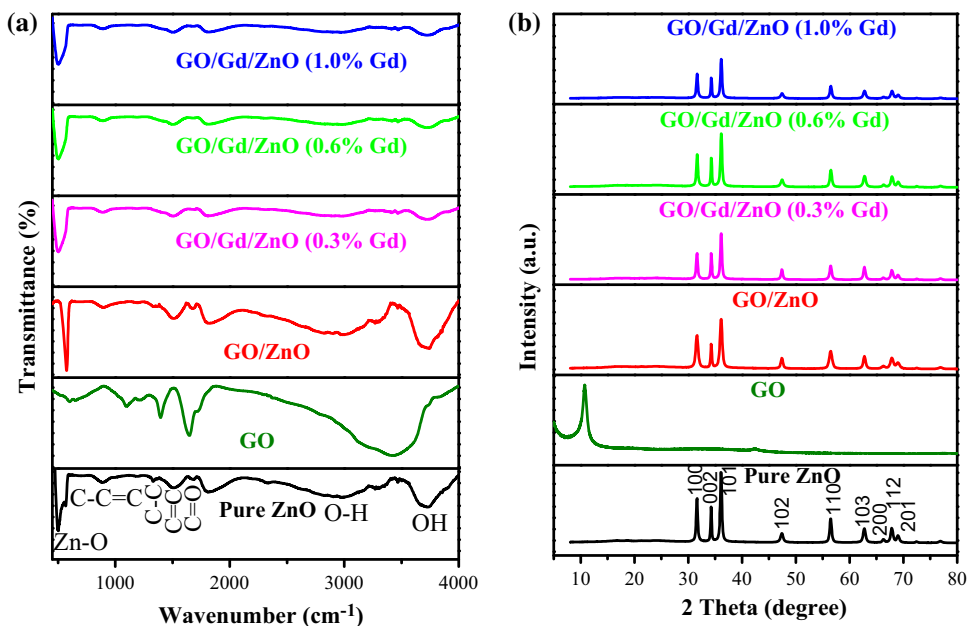
after immobilizing the Gd/ZnO and GO nanosheets in the composite framework, no characteristic peaks appeared, implying that Gd/ZnO and GO have the Zn–O vibration. Moreover, the FTIR spectra of GO/Gd/ZnO (with variable concentrations of Gd), exhibiting bands associated with ZnO and GO, confirmed the successful fabrication of the composite. The absorption band did not shift toward higher frequencies in the composites. This implied that the interactions between the Gd/ZnO and GO nanosheets increased to some degree. The GO spectra showing a broader band around 3435 cm^{-1} related to O–H stretching vibrations of the moisture absorbed on the samples [49]. The peak around 1732 and 1614 cm^{-1} was ascribed to carbonyl CO and C=O stretching, respectively, while the peaks at 1055 and 1420 cm^{-1} correspond to C–O epoxy group and carboxyl OH stretching at the edges of GO, respectively. The absorption bands at 1511 cm^{-1} confirmed that GO band was merged with the ZnO band in GO/Gd/ZnO composites. This indicates that GO has successfully modified znO.

Structure analysis

The phase composition and crystal structure of the as-synthesized samples were investigated using XRD analysis (Fig. 1b). XRD pattern of bulk ZnO and as-prepared GO/Gd/ZnO composites showed diffraction peaks at 31.81°, 34.47°, 35.98°, 47.59°, 57.52°,

63.18°, 66.39°, 68.01° and 69.10°, which was indexed to the (100), (002), (101), (102), (110), (103), (200), (112) and (201) planes. The observed diffraction peaks were well indexed to ZnO wurtzite structure [JCPDS No. 36–1451, space group: $P6_3mc$ (186)] [50]. GO showed a diffraction peak at $2\theta = 10.85°$ with a 0.77 nm interlayer distance, which corresponds to the (002) diffraction plane. This was similar to earlier studies [51–53]. The GO diffraction peak significantly larger than that found in the XRD pattern of pure graphite ($2\theta = 26°$) confirms the successful fabrication of GO. This could be rationalized by the presence of oxygenated functional groups on the carbon sheets of GO. Moreover, no diffraction peaks for GO could be observed in the GO/Gd/ZnO composites (with variable concentrations of Gd), which was due to the low amount and relatively low diffraction intensity of GO [54].

Raman spectroscopy technique was employed to offer knowledge on the chemical and structural properties including crystallinity and defects in the catalyst. The Raman spectra at 209, 331, 388, 437, and 571 cm^{-1} were indexed to typical active modes of ZnO [21] (Fig. 2).

The bands at 571 and 437 cm^{-1} were related to the A$_1$(LO) and E$_{2H}$ vibrational modes of hexagonal wurtzite phase of ZnO, respectively [55]. The E$_{2H}$ mode was attributed to oxygen deficiency defect and the A$_1$ (LO) mode was attributed to zinc-free carriers and the number of defects [21]. The bands at 388, 331

Figure 2 FTIR spectra of **a** ZnO and **b** GO, GO/ZnO and GO/Gd/ZnO composites. GO/Z1, GO/Z2 and GO/Z3 represent GO/Gd/ZnO (0.3% Gd), GO/Gd/ZnO (0.6% Gd) and GO/Gd/ZnO (1.0% Gd), respectively.
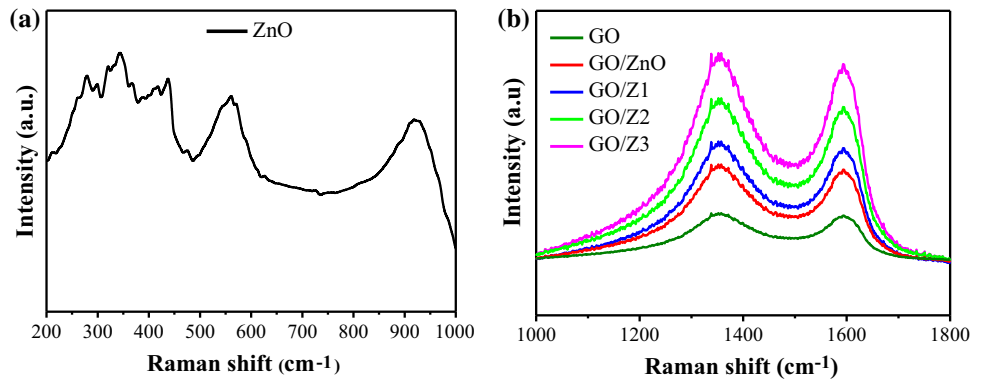
and 209 cm^{-1} were related to the E$_1$ (TO), 3E$_{2H}$-E$_{2L}$ and 2E$_{2L}$ modes, respectively [21]. The Raman spectra of the composites and GO show two vibrational modes at 1599 cm^{-1} (G band) and 1366 cm^{-1} (D band), see Fig. 2b. The G-band is commonly related to the sp^2 carbon E$_{2g}$-phonon, while the D-band is the A$_{1g}$ symmetry breathing mode of k-point phonons. The G-band provides details on the degree of graphitization, while the D-band suggests graphene disorder resulting from vacancy-related and grain boundary defects. The ratio of disordered (D) and graphitic (G) peaks determines the extent of surface defects. Raman spectroscopy facilitates the quantification of the carbonaceous phases by fitting the Raman spectra [56–58]. The D-band to G-band peak intensity ratio (I_D/I_G) is a measure of the defect accumulation in graphene sheets based on various degrees of reduction, and a smaller intensity of I_D/I_G ratio can be consigned to fewer sp^3 defects/disorders and better average size (or less amount) of the in-plane graphitic crystallite sp^2 domains [59]. The ID/IG ratio of GO/Gd/ZnO (0.3% Gd), GO/Gd/ZnO (0.6% Gd) and GO/Gd/ZnO (1.0% Gd) was 1.05, 1.04 and 1.02, respectively. The I_D/I_G values of the composites higher than that of GO signifying the formation of more sp^3 defects in carbon [60]. The increased sp^3 defects were due to the strong interaction between the interface of Gd/ZnO and GO.

TEM and SEM analysis

The TEM image of ZnO shows a spherical shape and possess regular/uniform size with an average crystallite size of 30 nm (Fig. 3a).

The TEM image of GO in Fig. 3b showed irregular and wrinkle characteristics. The TEM image (Fig. 3c) of GO/Gd/ZnO composites revealed that ZnO was packed compactly in the curled surface of GO sheets showing the successful formation of GO/Gd/ZnO composites. The EDX spectrum and mapping analysis revealed the occurrence of Zn, O, C and Gd atoms in the composites (Fig. 3f, g).

UV–Vis DRS analysis

UV–Vis diffuse reflectance spectra were used to assess the absorption properties of the as-fabricated catalyst. As given in Fig. 4a, bulk ZnO shows no absorption in the visible light region (400–700 nm).

The DRS-UV visible spectrum showed that the absorption wavelength of GO/ZnO composite was shifted to a slightly higher region when compared to bulk ZnO. This was because of the intimate contact between ZnO and GO, where the existence of GO reduced the reflectivity of the GO/ZnO composite to light. Moreover, the introduction of Gd improved the visible light absorption than that of bulk ZnO and GO/ZnO composite. The redshift of the absorption of GO/Gd/ZnO composites was mostly due to the loading of Gd ions in the ZnO crystal structure.

The disparity between the valence band and the conduction band gives the band gap energy (E_g) by which the as-prepared catalysts electronic structure is defined. The generation by as-prepared catalysts of reactive oxygen species, such as •O$_2^-$ and •OH, has been connected to the E_g and the redox potential of various reactive species. In general, the bandgap energy of semiconductor plays a vital influence on its photocatalytic performance. Therefore, we have assessed the optical band gap energy of photocatalysts from the following equation:

$$(\alpha h v)^{1/n} = A(h v - E_g), \tag{5}$$
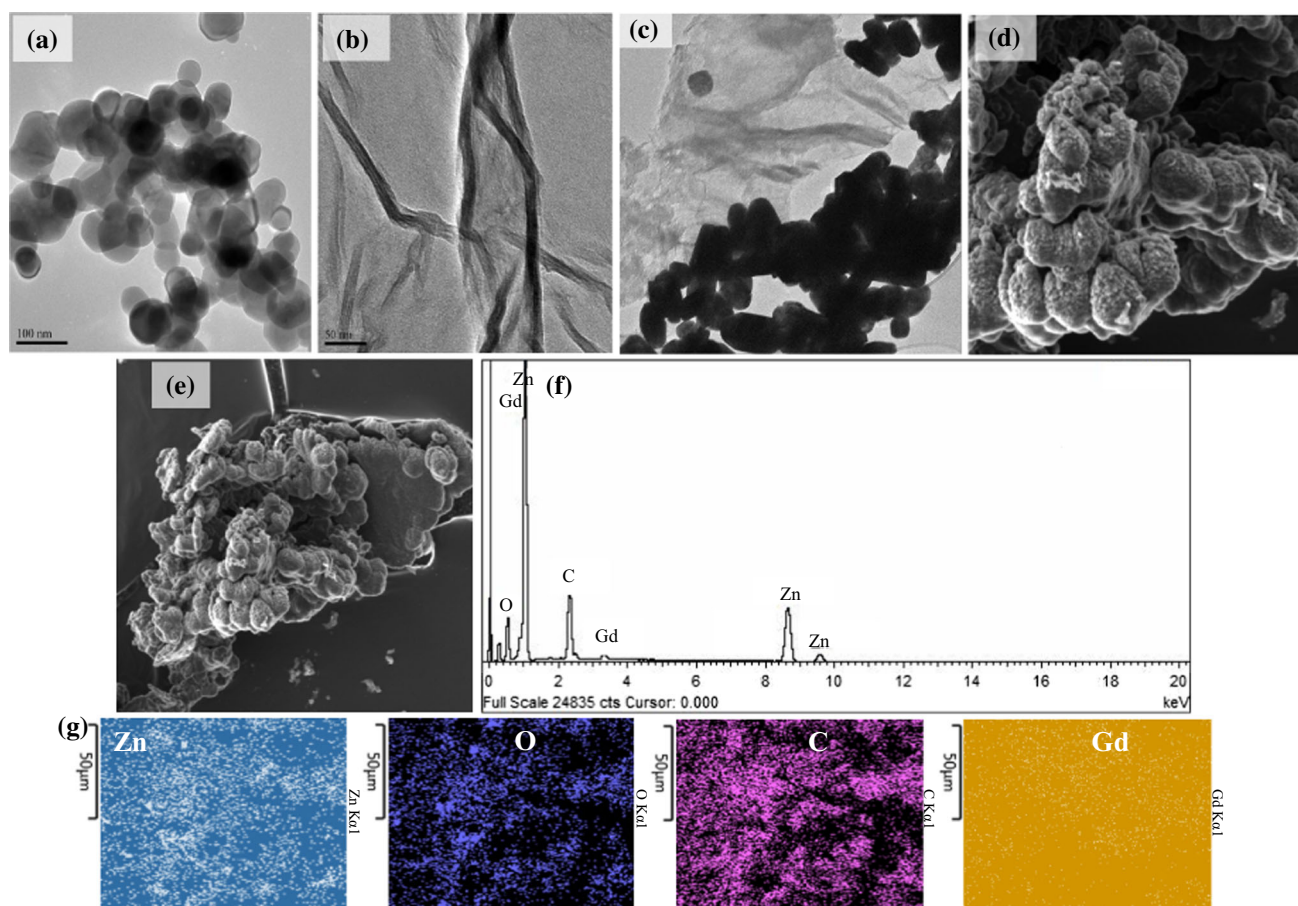
Figure 3 TEM images of **a** ZnO, **b** GO, **c** GO/Gd/ZnO composites; SEM images of **d** ZnO **e** GO/Gd/ZnO composites; **f** EDS of GO/Gd/ZnO composites and **g** elemental mapping of GO/Gd/ZnO composites for Zn, O, C and Gd.

where α, $h\nu$ and A are the absorption coefficient, photon energy and the proportionality constant, respectively [61]. The E_g energies of the as-prepared catalysts were calculated by measuring the x-axis intercept of an extrapolated tangential line from the linear regime of the curve. As shown in Fig. 4b, the E_g energies were estimated as 3.23, 3.18, 2.87, 2.79 and 2.94 eV for ZnO, GO/ZnO, GO/Gd/ZnO (0.3% Gd), GO/Gd/ZnO (0.6% Gd) and GO/Gd/ZnO (1.0% Gd), respectively. It could be seen that the addition of different amounts of Gd affects the E_g for GO/Gd/ZnO composites significantly than that of pure of ZnO. With the increase of Gd concentration, there was an increase in the E_g, which was in accordance with DRS. From the as-obtained results, it could be seen that the E_g value of GO/Gd/ZnO (0.6% Gd) decreases obviously as compared to that of GO/Gd/ZnO (0.3% Gd) and GO/Gd/ZnO (1.0% Gd) composites. This indicates that the GO/Gd/ZnO (0.6% Gd) composite could show higher photocatalytic

activity. This result indicated that Gd in GO/Gd/ZnO served as an electron acceptor, allowing the photoexcited electrons in ZnO to be transferred to GO via π electrons, which narrow the E_g [62]. Such a similar bandgap narrowing phenomenon has also been observed for other materials [27, 53, 63, 64], which is reflected by the optical property measurements of GO/Gd/ZnO composites, using the DRS.

The photoluminescence (PL) spectrum was employed to study the migration, separation and recombination behaviour of photogenerated charge carriers of the as-prepared samples. We observed similar peak positions with different intensities for the as-synthesized samples, as given in Fig. 4c. The addition of GO to ZnO led to fluorescence quenching, which reduces the recombination rate of charge carriers. The lower emission intensity observed for GO/Gd/ZnO composites revealed reduced recombination of charge carriers, where a suitable amount of Gd^{3+} ions loading could inhibit the recombination

Figure 4 a UV–Vis diffuse reflectance spectra, **b** plots of $(\alpha h\nu)^2$ versus photon energy $(h\nu)$ and **c** PL spectra of the as-prepared catalysts.
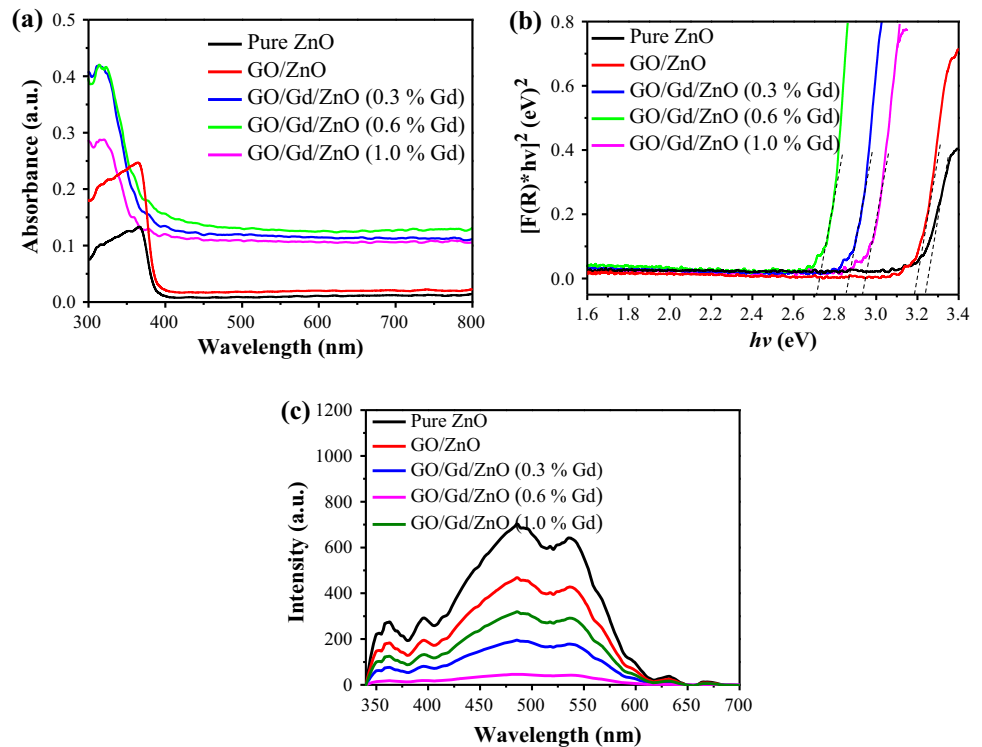

rate of charge carriers. Thus, in GO/Gd/ZnO composite, GO acted as an electrical pathway for the photogenerated electrons in ZnO, while Gd^{3+} ion could serve as an electron acceptor during the degradation process [37, 65]. Generally, a lower PL intensity resulted in a lower recombination rate of charge carriers and higher photoactivity [66]. Hence, GO/Gd/ZnO (0.6% Gd) with the lower PL intensity demonstrate that it had the highest electron transfer rate and its photoactivity could be higher than that of other composites.

DFT calculations were used to evaluate the electronic and structural properties of GO/ZnO and GO/Gd/ZnO composites. Both ZnO and GO sheets are known to be dynamically stable, which could be verified by calculating their phonon dispersion

curves. The phonon spectrum in Fig. 5 shows that the absence of imaginary frequencies in the entire Brillouin zone of ZnO and GO sheets indicates the dynamic stability of GO/ZnO and GO/Gd/ZnO composites.

To minimize the lattice mismatch between the stacking layers, the composites were built using 4×4 supercells of ZnO (Gd–ZnO) and 5×5 supercells of GO sheets. The small lattice mismatch (5.36%,) in the GO/ZnO and GO/Gd/ZnO composites was within the acceptable range of forming vdW composites. The interface adhesion energies of GO/ZnO and GO/Gd/ZnO composites were −0.376 and −0.366 meV Å^{-2}, respectively, indicating weak vdW interactions in the composites. The interface binding

Figure 5 Phonon dispersion plots of **a** ZnO **b** GO sheets.
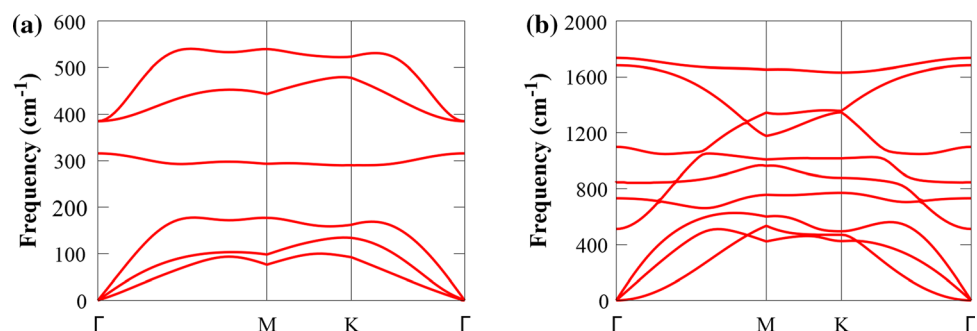
Figure 6 Side views of the optimized structures of **a** GO/ZnO and **b** GO/Gd/ZnO composites.
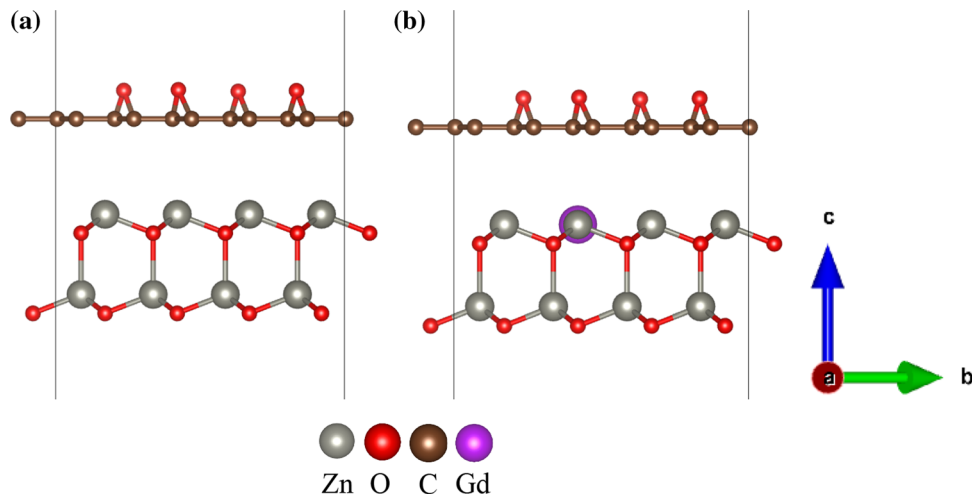
energies were all negative, signifying that both composites were stable (Fig. 6).

Besides the dynamical stability, the thermal stability of the composites was studied by evaluating the total energy fluctuation using the ab initio molecular dynamics (AIMD) simulations at 300 K. As shown in Fig. 7, the total energy oscillates with small fluctuations around a small range, which reveals the thermal stability of the composites at room temperature.

The interface binding energy, phonon and AIMD simulations confirm the structural stability of the composites. Therefore, it was reliably evident that both composites exhibited structural and thermodynamic stability, which confirmed successful fabrication.

To investigate the binding mechanism between ZnO (Gd/ZnO) and GO sheets, the electron localization functions (ELFs) were evaluated to confirm the existence of weak vdW forces. As shown in Fig. 8, no substantial charge accumulation at the interface indicates vdW interaction between the two components.

We have explored the charge transfer at the interface of the composite by calculating the charge density difference. The results are given in Fig. 9.

Figure 7 a Total energy (Ha) and **b** temperature (K) versus time (ps) for GO/ZnO and GO/Gd/ZnO composites.
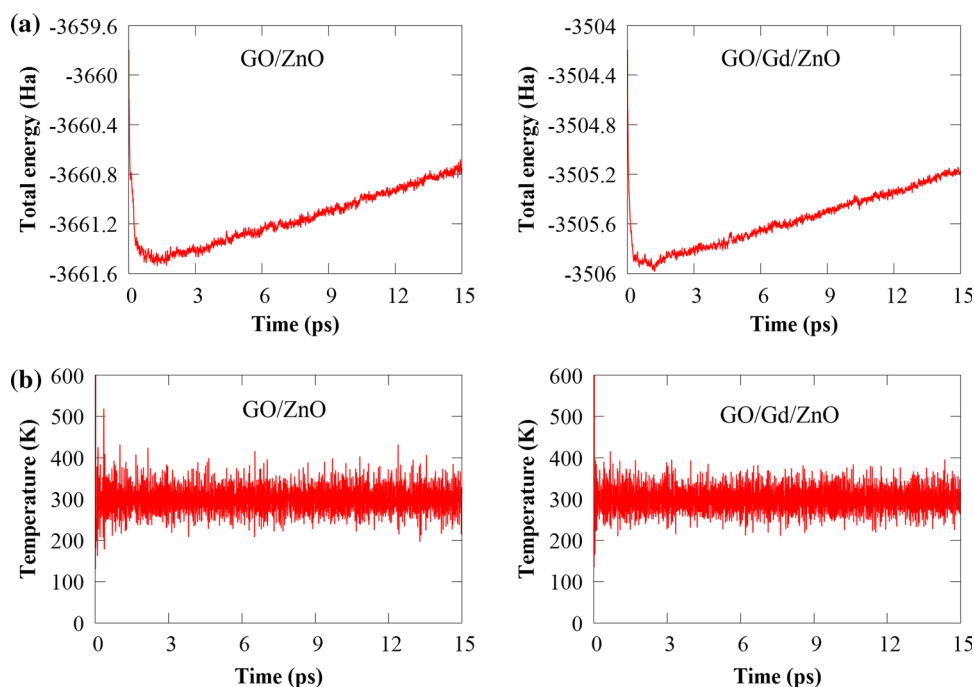
Figure 8 Electron localization functions of **a** GO/ZnO and **b** GO/Gd/ZnO composites.
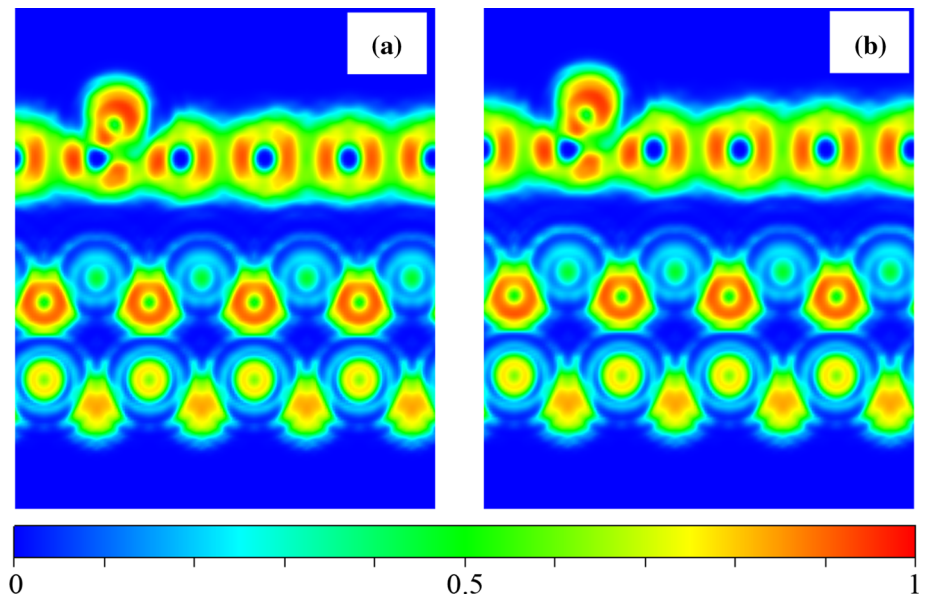
Figure 9 The charge density difference of **a** GO/ZnO and **b** GO/Gd/ZnO composites. The isosurface value is set to 0.0003 e Å^{-3}, where the loss and gain of electrons are represented by the blue and yellow areas, respectively.

Zn O C Gd
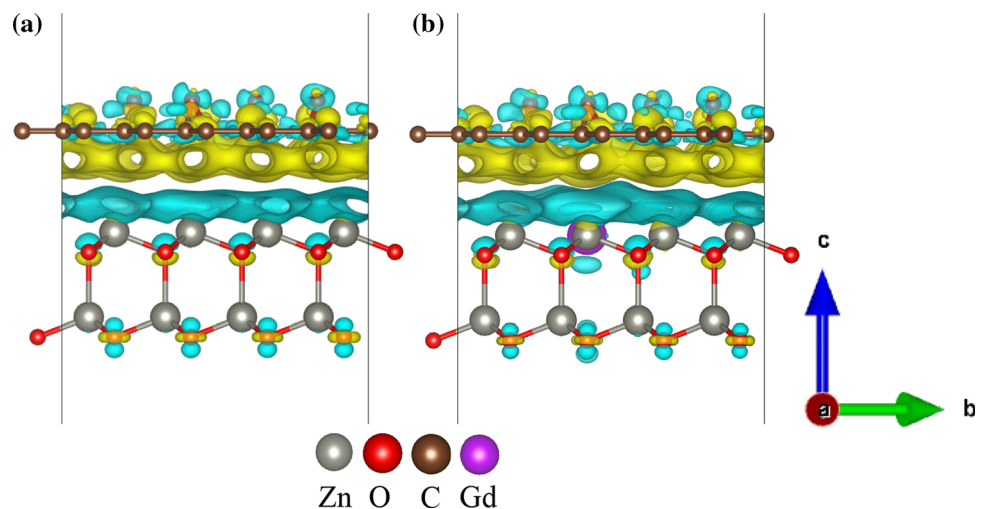
The blue (yellow) distribution represents charge depletion (accumulation). The electrons transfer to the GO sheets from ZnO (Gd–ZnO) and accumulate on the ZnO (Gd–ZnO) surface, while holes accumulate on the ZnO (Gd–ZnO) surface. This shows that composites formation results in charge transfer from the ZnO (Gd–ZnO) to GO sheets. Moreover, the Löwdin charge population analysis [67] was employed to evaluate the number of electrons transferred at the composite interface. We found that the number of electrons transferred from ZnO (Gd–ZnO) to GO sheets was 0.1301 (0.0425) $|e|$. Moreover, as shown in Fig. 10c and d, there was a potential drop of 9.94 (9.05) eV between the ZnO (Gd–ZnO) and GO sheets, suggesting the formation of a built-in electric field.

The reduced work function value of the composites than ZnO signifies the transfer of charge that took place at the interface.
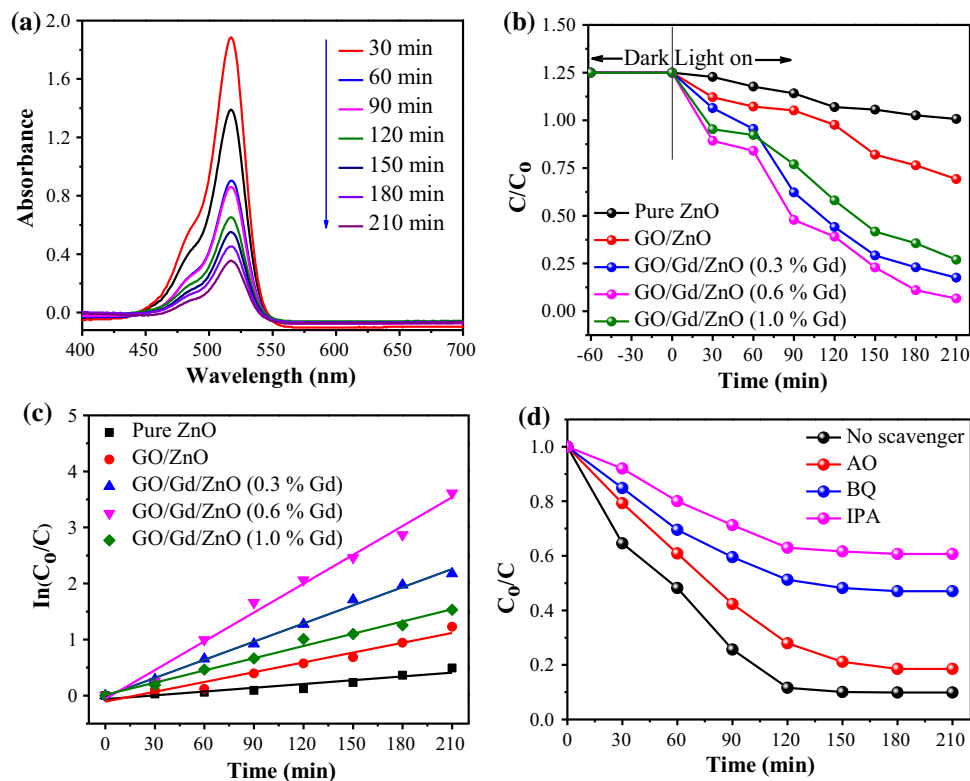
Photocatalytic performance evaluation

The as-prepared photocatalysts efficiency was assessed towards the degradation of environmental hazardous IC dye under simulated light illumination. The time-dependent UV–Vis spectra of IC dye during the UV light irradiation are shown in Fig. 11a. The IC dye maximum absorption peaks reduced gradually and disappeared completely under UV light illumination using GO/Gd/ZnO (0.6% Gd) photocatalyst.

Figure 10 Calculated electrostatic potentials along the z-direction of **a** ZnO, **b** GO, **c** GO/ZnO and **d** GO/Gd/ZnO composites.
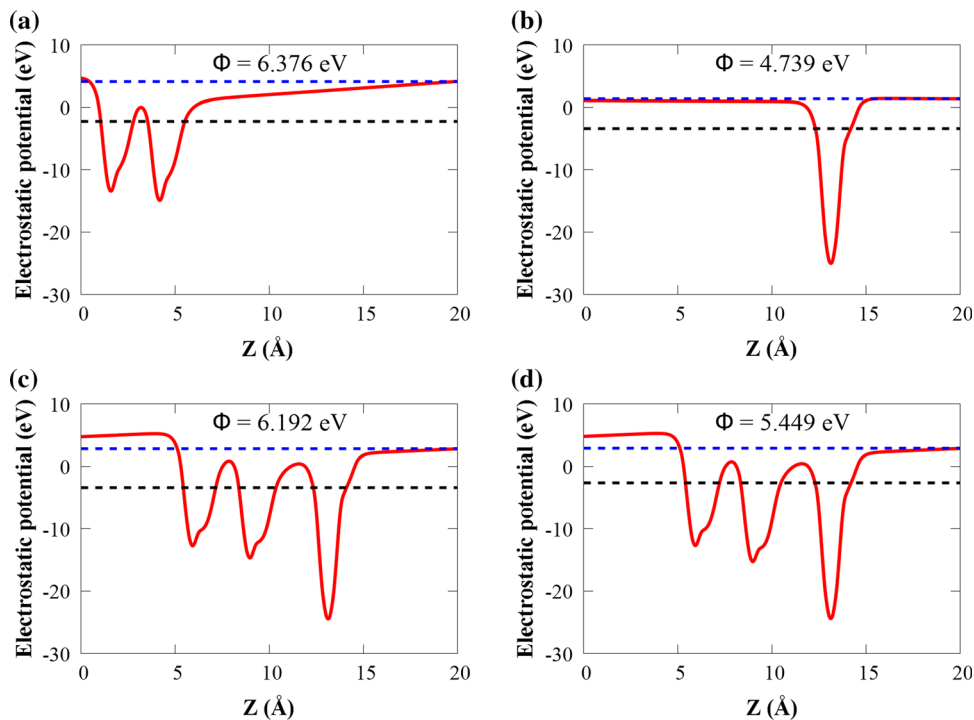
Figure 11 a Change in absorbance with time under UV light illumination using GO/Gd/ZnO (0.6% Gd) composite, **b** photodegradation efficiencies of IC dye in presence of different photocatalysts under UV light illumination, **c** kinetics of IC dye photodegradation [ln(C_0/C_t)] versus irradiation time and **d** effects of different scavengers on IC dye photocatalytic degradation using GO/Gd/ZnO (0.6% Gd) composite under UV light irradiation.

The photodegradation capacity of the as-prepared photocatalysts was assessed by evaluating the degradation of IC dye under UV light (Fig. 11b). Before irradiation to light, the IC dye absorption performance of the as-fabricated photocatalysts was performed in dark condition for 1 h. We observed that there was no dye adsorption in the dark condition. Moreover, the degradation performance of the

GO/ZnO photocatalysts was much better than that of bulk ZnO photocatalysts because of the electrostatic attraction of the surface functional groups, unique pore structure and large specific surface area of GO sheets. We observed that GO/Gd/ZnO photocatalysts showed higher degradation capability than bulk ZnO and GO/ZnO. The efficiency of pure ZnO, GO/ZnO, GO/Gd/ZnO (0.3% Gd) and GO/Gd/ZnO (1.0% Gd) for the photocatalytic degradation of IC dye was about 53, 69, 85 and 75%, respectively, after 210 min of light illumination. However, the photodegradation efficiency of GO/Gd/ZnO (0.6% Gd) photocatalysts was about 96% within 30 min of light irradiation, which was because of the lower bandgap energy, increased visible light absorption ability and synergistic effect between the GO and Gd/ZnO, indicating enhanced separation and transfer of photoexcited charge carriers. Hence, we also proved that the 0.6% Gd was the optimum concentration for the degradation of IC dye and GO/Gd/ZnO (0.6% Gd) composite was the ideal material for removing an organic pollutant from wastewater.

Moreover, the removal of IC dye by as-prepared photocatalysts with light irradiation was fitted to the pseudo-first-order kinetic model:

$$\ln(C/C_0) = -kt, \tag{6}$$

where C_0 and C (mg L^{-1}) are the concentrations of IC dye initially and after time (t) of exposure to light, respectively, and k is degradation rate constant. A plot of ln C/C_0 against reaction time t yields a straight line whose slope gives reaction rate constant. As revealed in Fig. 11c, the observed kinetics plots confirmed that the IC dye photocatalytic degradation follows a pseudo-first-order reaction. Obviously, GO/Gd/ZnO (0.6% Gd) (0.01713 min^{-1}) composite showed the largest degradation rate constant over all the materials, which was about 7.65, 2.94, 1.59 and 2.36 times higher than bulk ZnO (0.00224 min^{-1}), GO/ZnO (0.00583 min^{-1}), GO/Gd/ZnO (0.3% Gd) (0.01079 min^{-1}) and GO/Gd/ZnO (1.0% Gd) (0.00727 min^{-1}), respectively. This suggests that the introduction of GO on Gd/ZnO assists the separation and transfer of electron–hole pairs, thereby enhancing the photocatalytic performance and degradation efficiency of IC dye.

Detection of reactive oxidative species (ROS)

To understand the influence of reactive species during the photodegradation process, the effects of free radical capture were investigated to analyse the role of h$^+$, •O$_2^-$ and •OH in the IC dye photocatalytic degradation using GO/Gd/ZnO (0.6% Gd) photocatalysts. In the present work, BQ, IPA and AO were used as the quenchers for the $\cdot$O$_2^-$, $\cdot$OH and h$^+$, respectively. The results show in Fig. 11d indicate that the addition of BQ and IPA suppressed the photodegradation of IC dye using GO/Gd/ZnO (0.6% Gd) photocatalysts. The degradation rate of IC dye indicates that $\cdot$OH and $\cdot$O$_2^-$ radicals were both responsible for ROS during the photodegradation process. Moreover, the degradation of IC dye was slightly decreased when added into AO scavengers. This indicates that h$^+$ also significantly influences the degradation of IC dye in the presence of GO/Gd/ZnO (0.6% Gd) composite.

BET analysis

Generally, photocatalyst performance relied on the recombination of photogenerated charge carriers, BET specific surface area, and mean pore diameter [68]. N$_2$ adsorption–desorption measurements were explored to evaluate the specific surface area and the pore size distribution of the as-fabricated samples. The isothermal curves of N$_2$ adsorption–desorption in Fig. 12 showed a type IV curve with H$_2$ hysteresis loops, which reflect typical mesoporous materials.
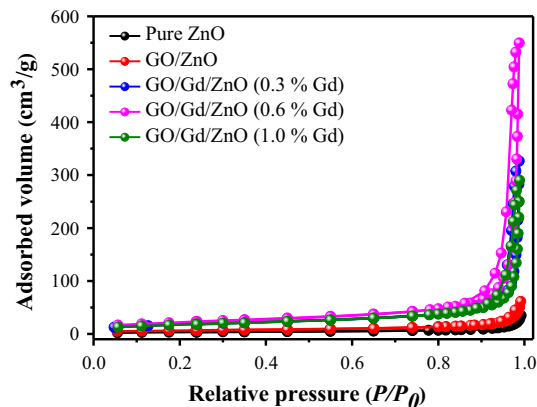
Figure 12 Nitrogen adsorption–desorption isotherms of the as-fabricated samples.

Table 1 BET specific surface area, pore volume and size of the as-fabricated samples

| Samples	BET surface area ($m^2\ g^{-1}$)	Mean pore size (nm)	Total pore volume ($cm^3\ g^{-1}$)
Pure ZnO	12.40	22.38	0.04
GO/ZnO	22.84	20.26	0.05
GO/Gd/ZnO (0.3% Gd)	64.54	37.35	0.16
GO/Gd/ZnO (0.6% Gd)	79.35	46.63	0.24
GO/Gd/ZnO (1.0% Gd)	63.57	33.47	0.14

For comparison, the BET surface area, mean pore size and total pore volume of the as-fabricated samples are listed in Table 1. The BET specific area of GO/Gd/ZnO (0.6% Gd) composite was higher than the other samples. Hence, the enhanced photocatalytic performance of GO/Gd/ZnO (0.6% Gd) composite than that of pure ZnO and other composites could be attributed to the increased BET specific area.

Stability and recyclability

Generally, the removal rate of total organic carbon (TOC) reflects the degree of mineralization of IC dye during the photocatalytic reaction. Apart from degradation, the mineralization of IC dye was ascertained using TOC analysis, as shown in Fig. 13a. The TOC removal concentration decreased steadily as the reaction time increases. At 180 min of irradiation of IC dye, much of the TOC was mineralized, suggesting the optimum reduction at 92%. This indicates the fragmentation of IC dye structure to form intermediates by reactive oxygen species, thereby enhancing mineralization during visible light irradiation. These intermediates would mineralize to form CO_2 and H_2O molecules.

The GO/Gd/ZnO photocatalyst reusability is a parameter of vital importance from the industrial perspective. After each photocatalytic cycle, the GO/Gd/ZnO was recovered from the reaction mixture by centrifugation, washed for each cycle and dried before starting the next cycle. The GO/Gd/ZnO recyclability was tested up to fifth cycle of IC dye degradation. Recycling experiments were performed in order to study the photostability of GO/Gd/ZnO photocatalyst under sunlight (Fig. 13b). We observed a slight steady reduction in the photocatalytic degradation efficiency with increasing runs, where the degradation of IC dye by GO/Gd/ZnO (0.6% Gd) composite remained above 80% even at the fifth cycle. This shows that even after the fifth cycle, GO/Gd/ZnO maintains good photoactivity for IC dye degradation. Moreover, it was observed that GO/Gd/ZnO did not show much loss of activity even after the fifth degradation cycle, suggesting that the catalyst was not photo-corroded during the reaction [69]. The minor weakening of the photocatalytic activity may be due to the partial occupancy of the active sites by the carbon deposits produced during the photodegradation of IC dyes on the catalyst surface [70].

Figure 13 **a** Mineralization of GO/Gd/ZnO (0.6% Gd) photocatalyst with time and **b** the recycling capacity of GO/Gd/ZnO (0.6% Gd) in the degradation of IC dye during five continuous runs under UV-light irradiation.
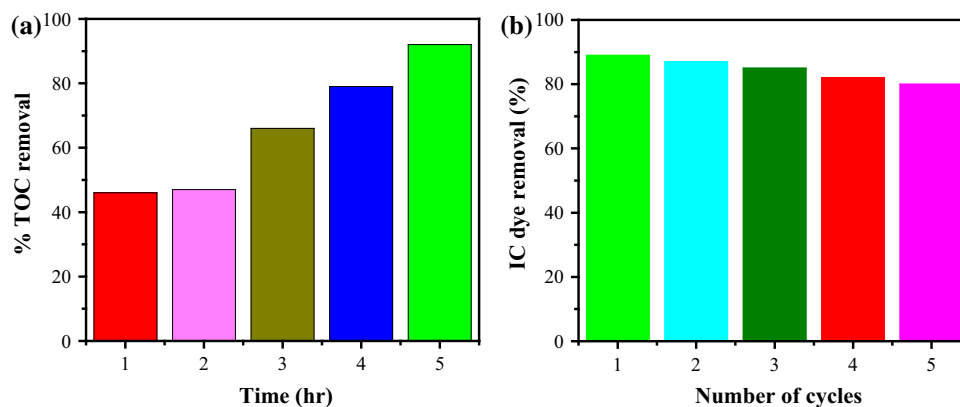
Conclusions

In summary, a novel GO/Gd/ZnO composite was fabricated successfully by a hydrothermal method and structurally characterize. The effect of Gd addition on GO/ZnO was assessed towards the degradation of IC dye under light illumination. All the photocatalytic experimental results show that the composites have high photocatalytic performance than that of bulk ZnO and GO/ZnO composite towards IC dye degradation, particularly, GO/Gd/ZnO (0.6% Gd), which could reach 96% complete degradation of IC dye in only 30 min. The results reveal that Gd ion could act as a bridge between GO and ZnO to enhance the separation of charge carriers and improve the photocatalytic removal rate of IC dye. Using the vdW-corrected DFT calculations, we have studied the structural, interfacial and electronic properties of GO/ZnO and GO/Gd/ZnO composites. The composites were confirmed to be stable by calculating its interfacial binding energy, vibrational phonon dispersion and AIMD simulations at 300 K. The interlayer vdWs contact was verified by calculating the electron localization functions. Moreover, we found from Löwdin charge population analysis that 0.1301 (0.0425) $|e|$ electrons transfer from ZnO (Gd–ZnO) to GO sheets at the interface, forming a built-in electric field pointing from ZnO (Gd–ZnO) to GO sheets with a potential drop (ΔV) of 9.94 (9.05) eV between the ZnO (Gd-ZnO) and GO sheets. The active species study reveals that $\cdot O_2^-$ and $\cdot OH$ radicals have a significant influence during the photodegradation process. Besides, the GO/Gd/ZnO composite was stable and could be easily recycled, which prove the reusability and reproducibility for photocatalytic pollutant degradation. This work offers new insights into preparing GO/Gd/ZnO catalysts with improve optical absorbance, photoluminescence quenching effect and increases surface area and is regarded as a suitable candidate for organic pollutants degradation in wastewater and other environmental remediation applications.

Acknowledgements

Compliance with ethical standards

Conflict of interest The authors declare that they have no conflict of interest.

References

[1] Herrera-García S, Aguirre-Ramírez M, Torres-Pérez J (2020) Comparison between Allura Red dye discoloration by activated carbon and azo bacteria strain. Environ Sci Pollut Res Int 27:29688–29696

[2] Oplatowska-Stachowiak M, Elliott CT (2017) Food colors: existing and emerging food safety concerns. Crit Rev Food Sci Nutr 57(3):524–548

[3] Hodges BC, Cates EL, Kim J-H (2018) Challenges and prospects of advanced oxidation water treatment processes using catalytic nanomaterials. Nat Nanotechnol 13(8):642–650

[4] Chequer FMD, Lizier TM, de Felício R, Zanoni MVB, Debonsi HM, Lopes NP, Marcos R, de Oliveira DP (2011) Analyses of the genotoxic and mutagenic potential of the products formed after the biotransformation of the azo dye Disperse Red 1. Toxicol In Vitro 25(8):2054–2063

[5] Chequer FMD, Lizier TM, de Felício R, Zanoni MVB, Debonsi HM, Lopes NP, de Oliveira DP (2015) The azo dye Disperse Red 13 and its oxidation and reduction products showed mutagenic potential. Toxicol In Vitro 29(7):1906–1915

[6] Cheng XQ, Zhang C, Wang ZX, Shao L (2016) Tailoring nanofiltration membrane performance for highly-efficient antibiotics removal by mussel-inspired modification. J Membr Sci 499:326–334

[7] Ding R, Zhang P, Seredych M, Bandosz TJ (2012) Removal of antibiotics from water using sewage sludge-and waste oil sludge-derived adsorbents. Water Res 46(13):4081–4090

[8] Cui J, Qi Y, Dong B, Mu L, Ding Q, Liu G, Jia M, Zhang F, Li C (2019) One-pot synthesis of $BaMg_{1/3}Ta_{2/3}O_{3-x}Ny/Ta_3N_5$ heterostructures as H_2-evolving photocatalysts for construction of visible-light-driven Z-scheme overall water splitting. Appl Catal B 241:1–7

[9] Uddin MT, Hoque ME, Chandra Bhoumick M (2020) Facile one-pot synthesis of heterostructure SnO_2/ZnO photocatalyst for enhanced photocatalytic degradation of organic dye. RSC Adv 10(40):23554–23565. https://doi.org/10.1039/D0RA03233F

[10] Uddin MT, Nicolas Y, Olivier C, Servant L, Toupance T, Li S, Klein A, Jaegermann W (2015) Improved photocatalytic activity in RuO_2–ZnO nanoparticulate heterostructures due to inhomogeneous space charge effects. Phys Chem Chem Phys 17(7):5090–5102

[11] Zhang X, Qin J, Hao R, Wang L, Shen X, Yu R, Limpanart S, Ma M, Liu R (2015) Carbon-doped ZnO nanostructures: facile synthesis and visible light photocatalytic applications. J Phys Chem C 119(35):20544–20554

[12] Wang J, Wang Z, Huang B, Ma Y, Liu Y, Qin X, Zhang X, Dai Y (2012) Oxygen vacancy induced band-gap narrowing and enhanced visible light photocatalytic activity of ZnO. ACS Appl Mater Interfaces 4(8):4024–4030

[13] Paul R, Gayen R, Biswas S, Bhat SV, Bhunia R (2016) Enhanced UV detection by transparent graphene oxide/ZnO composite thin films. RSC Adv 6(66):61661–61672

[14] Qian C, Yin J, Zhao J, Li X, Wang S, Bai Z, Jiao T (2020) Facile preparation and highly efficient photodegradation performances of self-assembled Artemia eggshell-ZnO nanocomposites for wastewater treatment. Colloids Surf Physicochem Eng Aspects 610:125752

[15] Wang H, Zhang L, Chen Z, Hu J, Li S, Wang Z, Liu J, Wang X (2014) Semiconductor heterojunction photocatalysts: design, construction, and photocatalytic performances. Chem Soc Rev 43(15):5234–5244

[16] Rambabu Y, Kumar U, Singhal N, Kaushal M, Jaiswal M, Jain SL, Roy SC (2019) Photocatalytic reduction of carbon dioxide using graphene oxide wrapped TiO_2 nanotubes. Appl Surf Sci 485:48–55

[17] Wang L, Li Z, Chen J, Huang Y, Zhang H, Qiu H (2019) Enhanced photocatalytic degradation of methyl orange by porous graphene/ZnO nanocomposite. Environ Pollut 249:801–811

[18] Kumar KVA, Lakshminarayana B, Suryakala D, Subrahmanyam C (2020) Reduced graphene oxide supported ZnO quantum dots for visible light-induced simultaneous removal of tetracycline and hexavalent chromium. RSC Adv 10(35):20494–20503. https://doi.org/10.1039/D0RA02062A

[19] Ge L, Zhang M, Wang R, Li N, Zhang L, Liu S, Jiao T (2020) Fabrication of CS/GA/RGO/Pd composite hydrogels for highly efficient catalytic reduction of organic pollutants. RSC Adv 10(26):15091–15097. https://doi.org/10.1039/D0RA01884H

[20] Xiang Q, Yu J, Jaroniec M (2012) Graphene-based semiconductor photocatalysts. Chem Soc Rev 41(2):782–796

[21] Zhu Z, Guo F, Xu Z, Di X, Zhang Q (2020) Photocatalytic degradation of an organophosphorus pesticide using a ZnO/rGO composite. RSC Adv 10(20):11929–11938. https://doi.org/10.1039/D0RA01741H

[22] Zeng B, Liu W, Zeng W (2019) Simple and environmentally-friendly synthesis of graphene–CdS hierarchical nanospheres and their photocatalytic performance. J Mater Sci Mater Electron 30(4):3753–3759. https://doi.org/10.1007/s10854-018-00657-3

[23] Li H, Wang P, Yi X, Yu H (2020) Edge-selectively amidated graphene for boosting H_2-evolution activity of TiO_2 photocatalyst. Appl Catal B 264:118504. https://doi.org/10.1016/j.apcatb.2019.118504

[24] Huang B (2017) Doping of RE ions in the 2D ZnO layered system to achieve low-dimensional upconverted persistent luminescence based on asymmetric doping in ZnO systems. Phys Chem Chem Phys 19(20):12683–12711. https://doi.org/10.1039/C7CP01623A

[25] Anandan S, Miyauchi M (2011) Ce-doped ZnO ($Ce_xZn_{1-x}O$) becomes an efficient visible-light-sensitive photocatalyst by co-catalyst (Cu^{2+}) grafting. Phys Chem Chem Phys 13(33):14937–14945. https://doi.org/10.1039/C1CP21514K

[26] Das T, Das BK, Parashar K, Kumar R, Choudhary HK, Anupama AV, Sahoo B, Sahoo PK, Parashar SKS (2017) Effect of Sr-doping on sinterability, morphology, structure, photocatalytic activity and AC conductivity of ZnO ceramics. J Mater Sci Mater Electron 28(18):13587–13595. https://doi.org/10.1007/s10854-017-7198-6

[27] Mahour LN, Choudhary HK, Kumar R, Anupama A, Sahoo B (2019) Structural, optical and Mössbauer spectroscopic investigations on the environment of Fe in Fe-doped ZnO ($Zn_{1-x}Fe_xO$) ceramics synthesized by solution combustion method. Ceram Int 45(18):24625–24634

[28] Anantharamaiah P, Chandra NS, Shashanka H, Kumar R, Sahoo B (2020) Magnetic and catalytic properties of Cu-substituted $SrFe_{12}O_{19}$ synthesized by tartrate-gel method. Adv Powder Technol 31(6):2385–2393

[29] Ray SK, Kshetri YK, Yamaguchi T, Kim T-H, Lee SW (2019) Characterization and multicolor upconversion emission properties of $BaMoO_4$: Yb^{3+}, Ln^{3+} (Ln= Tm, Ho, Tm/Ho) microcrystals. J Solid State Chem 272:87–95

[30] Khan M, Cao W (2013) Preparation of Y-doped TiO_2 by hydrothermal method and investigation of its visible light photocatalytic activity by the degradation of methylene blue. J Mol Catal A: Chem 376:71–77

[31] Xu W, Hu Y, Jin Z, Zheng L, Zhang Z, Cao W (2018) Anti-stokes excited Er^{3+}/Yb^{3+} codoped oxyfluoride glass ceramic for luminescence thermometry. J Lumin 203:401–408

[32] Jin X, Li H, Li D, Zhang Q, Li F, Sun W, Chen Z, Li Q (2016) Role of ytterbium-erbium co-doped gadolinium molybdate ($Gd_2(MoO_4)_3$: Yb/Er) nanophosphors in solar cells. Opt Express 24(18):A1276–A1287

[33] Ren S, Fan G, Liang M, Wang Q, Zhao G (2014) Electrodeposition of hierarchical ZnO/Cu_2O nanorod films for

highly efficient visible-light-driven photocatalytic applications. J Appl Phys 115(6):064301

[34] Marcano DC, Kosynkin DV, Berlin JM, Sinitskii A, Sun Z, Slesarev A, Alemany LB, Lu W, Tour JM (2010) Improved synthesis of graphene oxide. ACS Nano 4(8):4806–4814. https://doi.org/10.1021/nn1006368

[35] Oppong SO-B, Opoku F, Govender PP (2020) Remarkable enhancement of Eu–TiO$_2$–GO composite for photodegradation of indigo carmine: a design method based on computational and experimental perspectives. Catal Lett. https://doi.org/10.1007/s10562-020-03386-7

[36] Oppong SO-B, Opoku F, Anku WW, Kiarii EM, Govender PP (2019) Experimental and computational design of highly active Ce–ZrO$_2$–GO photocatalyst for eosin yellow dye degradation: the role of interface and Ce^{3+} ion. Catal Lett 149(6):1633–1650. https://doi.org/10.1007/s10562-019-02729-3

[37] Oppong SO-B, Opoku F, Govender PP (2019) Tuning the electronic and structural properties of Gd–TiO$_2$–GO nanocomposites for enhancing photodegradation of IC dye: the role of Gd^{3+} ion. Appl Catal, B 243:106–120. https://doi.org/10.1016/j.apcatb.2018.10.031

[38] Oppong SOB, Anku WW, Opoku F, Shukla SK, Govender PP (2018) Photodegradation of eosin yellow dye in water under simulated solar light irradiation using La-doped ZnO nanostructure decorated on graphene oxide as an advanced photocatalyst. ChemistrySelect 3(4):1180–1188

[39] Giannozzi P, Andreussi O, Brumme T, Bunau O, Nardelli MB, Calandra M, Car R, Cavazzoni C, Ceresoli D, Cococcioni M (2017) Advanced capabilities for materials modelling with Quantum ESPRESSO. J Phys: Condens Matter 29(46):465901

[40] Giannozzi P, Baroni S, Bonini N, Calandra M, Car R, Cavazzoni C, Ceresoli D, Chiarotti GL, Cococcioni M, Dabo I (2009) QUANTUM ESPRESSO: a modular and open-source software project for quantum simulations of materials. J Phys: Condens Matter 21(39):395502

[41] Hamann D (2013) Optimized norm-conserving Vanderbilt pseudopotentials. Phys Rev B 88(8):085117

[42] Perdew JP, Burke K, Ernzerhof M (1996) Generalized gradient approximation made simple. Phys Rev Lett 77(18):3865–3868

[43] Grimme S, Antony J, Ehrlich S, Krieg H (2010) A consistent and accurate ab initio parametrization of density functional dispersion correction (DFT-D) for the 94 elements H-Pu. J Chem Phys 132(15):154104

[44] Pack JD, Monkhorst HJ (1977) "Special points for Brillouin-zone integrations": a reply. Phys Rev B 16(4):1748–1749. https://doi.org/10.1103/PhysRevB.16.1748

[45] Head JD, Zerner MC (1985) A Broyden–Fletcher–Goldfarb–Shanno optimization procedure for molecular geometries. Chem Phys Lett 122(3):264–270. https://doi.org/10.1016/0009-2614(85)80574-1

[46] Baroni S, de Gironcoli S, Dal Corso A, Giannozzi P (2001) Phonons and related crystal properties from density-functional perturbation theory. Rev Mod Phys 73(2):515–562. https://doi.org/10.1103/RevModPhys.73.515

[47] Momma K, Izumi F (2011) VESTA 3 for three-dimensional visualization of crystal, volumetric and morphology data. J Appl Crystallogr 44(6):1272–1276. https://doi.org/10.1107/S0021889811038970

[48] Yang J, Zang C, Sun L, Zhao N, Cheng X (2011) Synthesis of graphene/Ag nanocomposite with good dispersibility and electroconductibility via solvothermal method. Mater Chem Phys 129(1):270–274. https://doi.org/10.1016/j.matchemphys.2011.04.002

[49] Zangmeister CD (2010) Preparation and evaluation of graphite oxide reduced at 220 °C. Chem Mater 22(19):5625–5629. https://doi.org/10.1021/cm102005m

[50] Madsen IC, Scarlett NV, Cranswick LM, Lwin T (2001) Outcomes of the International Union of Crystallography Commission on powder diffraction round robin on quantitative phase analysis: samples 1a to 1h. J Appl Crystallogr 34(4):409–426

[51] Yadav A, Kumar R, Choudhary HK, Sahoo B (2018) Graphene-oxide coating for corrosion protection of iron particles in saline water. Carbon 140:477–487. https://doi.org/10.1016/j.carbon.2018.08.062

[52] Yadav A, Kumar R, Pandey UP, Sahoo B (2021) Role of oxygen functionalities of GO in corrosion protection of metallic Fe. Carbon 173:350–363. https://doi.org/10.1016/j.carbon.2020.11.029

[53] Kumar R, Kumar A, Verma N, Khopkar V, Philip R, Sahoo B (2020) Ni nanoparticles coated with nitrogen-doped carbon for optical limiting applications. ACS Appl Nano Mater 3(9):8618–8631

[54] Zhang Y, Zhang N, Tang Z-R, Xu Y-J (2012) Graphene transforms wide band gap ZnS to a visible light photocatalyst. The new role of graphene as a macromolecular photosensitizer. ACS Nano 6(11):9777–9789

[55] Kazeminezhad I, Saadatmand S, Yousefi R (2016) Effect of transition metal elements on the structural and optical properties of ZnO nanoparticles. Bull Mater Sci 39(3):719–724

[56] Kumar R, Sahoo B (2018) Investigation of disorder in carbon encapsulated core-shell Fe/Fe$_3$C nanoparticles synthesized by one-step pyrolysis. Diamond Relat Mater 90:62–71. https://doi.org/10.1016/j.diamond.2018.10.003

[57] Kumar R, Kumar A, Verma N, Anupama AV, Philip R, Sahoo B (2019) Modulating non-linear optical absorption through controlled graphitization of carbon nanostructures containing Fe_3C-graphite core-shell nanoparticles. Carbon 153:545–556. https://doi.org/10.1016/j.carbon.2019.07.058

[58] Kumar R, Manjunatha M, Anupama A, Ramesh K, Sahoo B (2019) Synthesis, composition and spin-dynamics of FCC and HCP phases of pyrolysis derived Co-nanoparticles embedded in amorphous carbon matrix. Ceram Int 45(16):19879–19887

[59] Luo D, Zhang G, Liu J, Sun X (2011) Evaluation criteria for reduced graphene oxide. J Phys Chem C 115(23):11327–11335

[60] Stankovich S, Dikin DA, Piner RD, Kohlhaas KA, Kleinhammes A, Jia Y, Wu Y, Nguyen ST, Ruoff RS (2007) Synthesis of graphene-based nanosheets via chemical reduction of exfoliated graphite oxide. Carbon 45(7):1558–1565

[61] Davis EA, Mott NF (1970) Conduction in non-crystalline systems V Conductivity, optical absorption and photoconductivity in amorphous semiconductors. Philos Mag 22(179):0903–0922. https://doi.org/10.1080/14786437008221061

[62] Alamdari S, Ghamsari MS, Afarideh H, Mohammadi A, Geranmayeh S, Tafreshi MJ, Ehsani MH (2019) Preparation and characterization of GO–ZnO nanocomposite for UV detection application. Opt Mater 92:243–250

[63] Kumar R, Kumar A, Verma N, Philip R, Sahoo B (2020) Mechanistic insights into the optical limiting performance of carbonaceous nanomaterials embedded with core–shell type graphite encapsulated Co nanoparticles. Phys Chem Chem Phys 22(46):27224–27240. https://doi.org/10.1039/D0CP03328F

[64] Kumar A, Kumar R, Verma N, Anupama AV, Choudhary HK, Philip R, Sahoo B (2020) Effect of the band gap and the defect states present within band gap on the non-linear optical absorption behaviour of yttrium aluminium iron garnets. Opt Mater 108:110163. https://doi.org/10.1016/j.optmat.2020.110163

[65] Madolappa S, Anupama A, Jaschin P, Varma K, Sahoo B (2016) Magnetic and ferroelectric characteristics of Gd^{3+} and Ti^{4+} co-doped $BiFeO_3$ ceramics. Bull Mater Sci 39(2):593–601

[66] Thiruppathi M, Senthil Kumar P, Devendran P, Ramalingan C, Swaminathan M, Nagarajan ER (2018) Ce@TiO_2 nanocomposites: an efficient, stable and affordable photocatalyst for the photodegradation of diclofenac sodium. J Alloys Compd 735:728–734. https://doi.org/10.1016/j.jallcom.2017.11.139

[67] Sanchez-Portal D, Artacho E, Soler JM (1995) Projection of plane-wave calculations into atomic orbitals. Solid State Commun 95(10):685–690

[68] Bhattacharjee A, Ahmaruzzaman M, Sinha T (2015) A novel approach for the synthesis of SnO_2 nanoparticles and its application as a catalyst in the reduction and photodegradation of organic compounds. Spectrochim Acta, Part A 136:751–760. https://doi.org/10.1016/j.saa.2014.09.092

[69] Deng Y, Tang L, Feng C, Zeng G, Wang J, Zhou Y, Liu Y, Peng B, Feng H (2018) Construction of plasmonic Ag modified phosphorous-doped ultrathin g-C_3N_4 nanosheets/$BiVO_4$ photocatalyst with enhanced visible-near-infrared response ability for ciprofloxacin degradation. J Hazard Mater 344:758–769

[70] Wang L, Ding J, Chai Y, Liu Q, Ren J, Liu X, Dai W-L (2015) CeO_2 nanorod/g-C_3N_4/N-rGO composite: enhanced visible-light-driven photocatalytic performance and the role of N-rGO as electronic transfer media. Dalton Trans 44(24):11223–11234. https://doi.org/10.1039/C5DT01479D